Piecewise Modelled Impact Resonator for Energy Harvesting Systems

Boyang Fu†, Elena Blokhina†, Diarmuid O'Connell†, Orla Feely† and Ronan Frizzell‡

†School of Electrical, Electronic and Communications Engineering,
University College Dublin, Ireland
‡Efficient Energy Transfer Department, Bell Labs, Alcatel-Lucent,
Blanchardstown Business & Tech. Pk, Dublin 15, Ireland.
Email: boyang.fu@ucdconnect.ie

Abstract—In this work, a novel resonator model with Coulomb damping has been developed. Fitting analysis between simulation results and experimental data shows that the proposed model exhibits better performance compared to the conventional mass-spring with viscous dampers model. The piecewise characteristics existing in the proposed model also show a rich variety of nonlinear behaviour.

1. Introduction

Applying multiple degrees of freedom (MDOF) design concepts to dynamic vibration absorbers has been previously used to achieve a number of performance improvements. For instance, MDOF was introduced into the vibratory micromachined gyroscopes in [1], which achieves a six times larger bandwidth than a conventional single mass system. Furthermore, [2] shows by using 2-DOF design, the micromachined gyroscopes can also be expected to yield reliable, robust and low-cost for high-volume applications.

[3] improved the piezoelectric VEH efficiency by introducing additional masses, which make use of multiple resonant frequencies. [4] presented numerical examples to illustrate that with proper selection of the design parameters of the 2-DOF resonator, the harvested power can be amplified by a factor of 20 as compared to the conventional 1-DOF resonator and the effective bandwidth of the harvester can be widened 25%.

However, current numerical models used in multi-DOF resonator analysis neglect some small term, such as gravity, viscous friction either caused by surrounding air or spring structure itself and dry friction caused by the device's supportive structures.

In this work, we develop a more accurate model for improved estimation of multi-DOF VEH behaviour. The 2-DOF resonator presented in this work is inspired by the vibration energy harvester reported in [5].

2. Model Description

The 2-DOF resonator consists of two mass-spring systems arranged in series as shown in Fig.1a, where the two springs have stiffness k_1 and k_2. When spring k_2 is transferring load to mass m_1 we describe the resonator as undergoing attached-vibration. In our design, the connection between spring k_2 and mass m_1 is not solid, meaning that spring k_2 cannot undergo tensile loading and mass m_2 can be separated from mass m_1 during vibration, as shown in Fig.1b. We describe the resonator working in this phase of operation as undergoing detached-vibration. Mechanical damping in Fig.1 consists of two parts: spring viscous structural damping c_1 and c_2 and viscous air damping b_1 and b_2. The mass supporting structure introduces an additional frictional damping factor that is discussed in Section 2.2.

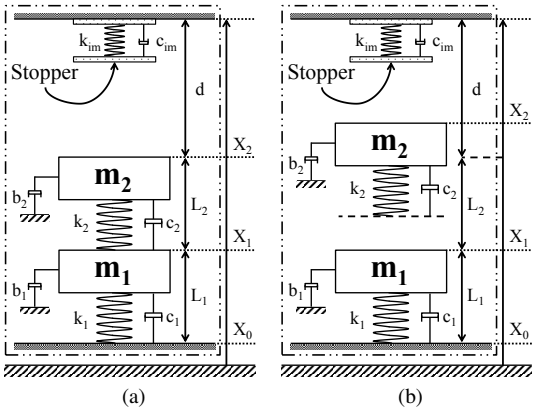

Figure 1: Schematic of the 2-DOF resonator working in different region: (a) attached-vibration and (b) detached-vibration modes of operation.

Table 1: Measured characteristics of the resonator

m_1	k_1	$f_{n,1}$	L_1	d
58.31 g	1.23 N/mm	23.1 Hz	43 mm	12 mm
m_2	k_2	$f_{n,2}$	L_2	k_{im}
4.75 g	0.36 N/mm	43.8 Hz	23.5 mm	0.36 N/mm

One extra spring k_{im} with damping factor c_{im} is fixed on the top of the package acting as end-stopper to protect the device. L_1 and L_2 are the length of two springs plus the thickness of two masses respectively. d is the gap between mass m_2 and the end-stopper.

Table 1 summarizes the measured characteristics of the resonator, where $f_{n,1}$ and $f_{n,2}$ are the natural frequencies of mass-spring systems m_1-k_1 and m_2-k_2 respectively.

2.1. Conventional Model

The conventional 2-DOF model consists of two mass-spring systems and viscous dampers representing air and structural damping.

The movements of the masses are constrained within one dimension, noted axis X. X_0, X_1 and X_2 are the absolute displacement of the moving base, mass m_1 and mass m_2 with respect to a fixed ground respectively. The system governing equation for attached-vibration can be written as below:

$$\begin{cases} m_1\ddot{X}_1 = -k_1(X_1 - X_0 - L_1) - c_1(\dot{X}_1 - \dot{X}_0) \\ \qquad\quad +k_2(X_2 - X_1 - L_2) + c_2(\dot{X}_2 - \dot{X}_1) \\ \qquad\quad -b_1(\dot{X}_1 - \dot{X}_0) - m_1 g \\ m_2\ddot{X}_2 = -k_2(X_2 - X_1 - L_2) - c_2(\dot{X}_2 - \dot{X}_1) \\ \qquad\quad -b_2(\dot{X}_2 - \dot{X}_0) - m_2 g - F_{im} \end{cases} \tag{1}$$

where $c_1(\dot{X}_1 - \dot{X}_0)$ and $c_2(\dot{X}_2 - \dot{X}_1)$ are the spring damping force [5], $b_1(\dot{X}_1 - \dot{X}_0)$ and $b_2(\dot{X}_2 - \dot{X}_0)$ are air damping force [6], F_{im} is the end-stopper force, and $g = 9.8m/s^2$ is the gravitational acceleration.

The base movement is represented as $\ddot{X}_0 = A_{ext}\sin(\omega_{ext}t + \vartheta_0)$, where A_{ext}, ω_{ext} and ϑ_0 are the amplitude, angular frequency and initial phase respectively. We define new variables:

$$x_1 = X_1 - X_0 - L_1 \text{ and } x_2 = X_2 - X_0 - L_2 - L_1 \tag{2}$$

and substituting (2) into (1) for the attached case gives:

$$\begin{cases} m_1\ddot{x}_1 = -k_1x_1 - c_1\dot{x}_1 - m_1A_{ext}\sin(\omega_{ext}t + \vartheta_0) \\ \qquad\quad -b_1\dot{x}_1 + k_2(x_2 - x_1) + c_2(\dot{x}_2 - \dot{x}_1) - m_1 g \\ m_2\ddot{x}_2 = -k_2(x_2 - x_1) - c_2(\dot{x}_2 - \dot{x}_1) - b_2\dot{x}_2 - m_2 g \\ \qquad\quad -m_2A_{ext}\sin(\omega_{ext}t + \vartheta_0) - F_{im} \end{cases} \tag{3a}$$

Correspondingly, the governing equation for detached-vibration shown in Fig.1b can be written as:

$$\begin{cases} m_1\ddot{x}_1 = -k_1x_1 - c_1\dot{x}_1 - b_1\dot{x}_1 - m_1 g \\ \qquad\quad -m_1A_{ext}\sin(\omega_{ext}t + \vartheta_0) \\ m_2\ddot{x}_2 = -b_2\dot{x}_2 - m_2 g - F_{im} \\ \qquad\quad -m_2A_{ext}\sin(\omega_{ext}t + \vartheta_0) \end{cases} \tag{3b}$$

Note that the interaction between m_1 and m_2 has been removed compared to (3a).

The end stopper force F_{im} can be described as follow:

$$F_{im} = \begin{cases} k_{im}(x_2 - d) + c_{im}\dot{x}_2 & \text{if } (x_2 - d) > 0 \\ 0 & \text{if } (x_2 - d) \le 0 \end{cases} \tag{4}$$

From the description above we can get the system piecewise condition that determines attached and detached conditions as $x_2 - x_1 = 0$. Thus, we get:

$$\text{System Governing Eq.} \begin{cases} \text{Eq.}(3a) & \text{if } (x_2 - x_1) \le 0 \\ \text{Eq.}(3b) & \text{if } (x_2 - x_1) > 0 \end{cases} \tag{5}$$

2.2. Model with Coulomb Damping

In the real experimental setup, the basic holding support for the resonator is a non-magnetic metallic central rod and each mass has a guide hole through the middle. The masses can hit the central rod so the dry friction (Coulomb damping) can be generated from the interaction of the masses and central rod. This dry friction force is a function of the normal force applied by the central rod against the masses and in a direction opposite to relative speed between them. For simplifying the analysis, assuming the dry friction force can be represented as:

$$\begin{cases} F_{D,1} = \overline{F}_{f,1} \cdot \text{sgn}(\dot{x}_1) \\ F_{D,2} = \overline{F}_{f,2} \cdot \text{sgn}(\dot{x}_2) \end{cases} \tag{6}$$

where $\overline{F}_{f,1}$ and $\overline{F}_{f,2}$ are the average dry friction force applied to mass m_1 and m_2 respectively. So we can rewrite (3) as below:

$$\begin{cases} m_1\ddot{x}_1 = -k_1x_1 - c_1\dot{x}_1 - b_1\dot{x}_1 - \overline{F}_{f,1} \cdot \text{sgn}(\dot{x}_1) \\ \qquad\quad -m_1A_{ext}\sin(\omega_{ext}t + \vartheta_0) - m_1 g \\ \qquad\quad +k_2(x_2 - x_1) + c_2(\dot{x}_2 - \dot{x}_1) \\ m_2\ddot{x}_2 = -k_2(x_2 - x_1) - c_2(\dot{x}_2 - \dot{x}_1) - b_2\dot{x}_2 \\ \qquad\quad -m_2A_{ext}\sin(\omega_{ext}t + \vartheta_0) - m_2 g \\ \qquad\quad -F_{im} - \overline{F}_{f,2} \cdot \text{sgn}(\dot{x}_2) \end{cases} \tag{7a}$$

$$\begin{cases} m_1\ddot{x}_1 = -k_1x_1 - c_1\dot{x}_1 - b_1\dot{x}_1 - \overline{F}_{f,1} \cdot \text{sgn}(\dot{x}_1) \\ \qquad\quad -m_1A_{ext}\sin(\omega_{ext}t + \vartheta_0) - m_1 g \\ m_2\ddot{x}_2 = -m_2A_{ext}\sin(\omega_{ext}t + \vartheta_0) - m_2 g \\ \qquad\quad -F_{im} - \overline{F}_{f,2} \cdot \text{sgn}(\dot{x}_2) - b_2\dot{x}_2 \end{cases} \tag{7b}$$

And we have:

$$\text{System Governing Eq.} \begin{cases} \text{Eq.}(7a) & \text{if } (x_2 - x_1) \le 0 \\ \text{Eq.}(7b) & \text{if } (x_2 - x_1) > 0 \end{cases} \tag{8}$$

2.3. Parameter Fitting

The damping coefficients were derived through fitting analysis between the theoretical model simulation results and the experimental results. The displacement data were measured by a laser displacement gauge outside the device. Due to the constraint of the measuring instruments, we use absolute displacement here. Due to the rich nonlinear behaviour existing in this system, we use RMS displacement value to evaluate the fitting results. The experiments are performed under two acceleration levels, i.e. $A_{ext} = 0.3$g and $A_{ext} = 0.5$g, over the 12Hz to 30Hz (1Hz step) external frequency range.

Table 2 summarizes the derived characteristics of the resonator. b_1 and c_1 have the same impact in the equations. In the model with dry friction, the air damping force applied to mass m_2 is totally overwhelmed by the Coulomb damping force $\overline{F}_{f,2}$, thus b_2 can be neglected in this model.

Fig.2 to Fig.4 show the fitted results for the three cases listed in table 2 respectively. The set 1 conventional model fitting parameters were optimized for $A_{ext} = 0.3$g conditions. As can be seen in Fig.2 the simulation and experimental matching accuracy for the m_2 RMS displacement is comparable while the matching accuracy for m_1 is poor. The set 2 conventional model parameters are optimized for $A_{ext} = 0.5$g conditions and Fig.3 show an improved matching accuracy for the $A_{ext} = 0.5$g case.

We estimate the fitting performance by calculating the sum of the squares of the errors defining as below:

Table 2: Fitting parameters of the resonator

	Unit	Conventional Model		Model with Dry Friction
		Set 1	Set 2	
$b_1 + c_1$	N · s/m	2	1.6	0.8
c_2	N · s/m	0.1	0.08	0.1
b_2	N · s/m	0.03	0.025	0
$\overline{F}_{f,1}$	N	N/A		0.08
$\overline{F}_{f,2}$	N	N/A		0.002

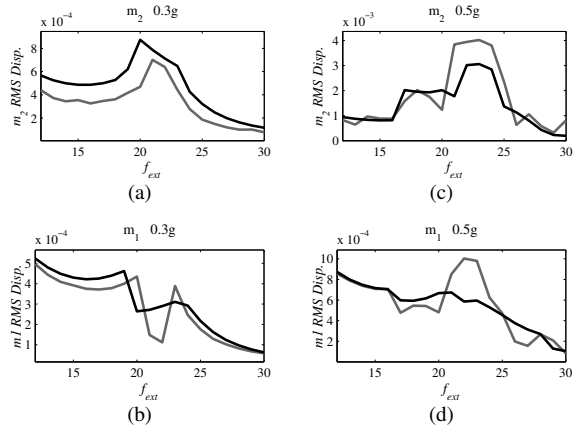

Figure 2: Fitting results of parameters set 1 of conventional model. Grey lines represent experimental data and black lines are simulation results. (a) m_2 under A_{ext} = 0.3 g, (b) m_1 under A_{ext} = 0.3 g, (c) m_2 under A_{ext} = 0.5 g, (d) m_1 under A_{ext} = 0.5 g.

$$S = \sum(\chi_{\text{sim,m1}} - \chi_{\text{raw,m1}})^2 + \sum(\chi_{\text{sim,m2}} - \chi_{\text{raw,m2}})^2 \quad (9)$$

where χ_{sim} is the RMS displacement calculated from simulation results and χ_{raw} is the RMS displacement derived from experimental results.

Table 3 summarizes the relative error S of each case.

Table 3: Relative error of each fitting set

	Conventional Model		Model with Dry Friction
	Set 1	Set 2	
A_{ext} = 0.3 g	1.39	7.29	1.06
A_{ext} = 0.5 g	1.06	0.46	0.41

The fitting results illustrate that the model with Coulomb damping is superior to the conventional model. The model with Coulomb damping not only shows closer agreement between experimental and simulation results for both acceleration levels examined, but achieves these results using the same fitting parameters, which is a significant improvement over the conventional model performance.

3. Chaotic Behaviour

Due to the switching between the different configurations, i.e. attached-vibration and detached-vibration, the proposed 2-DOF resonator can present rich nonlinear behaviour.

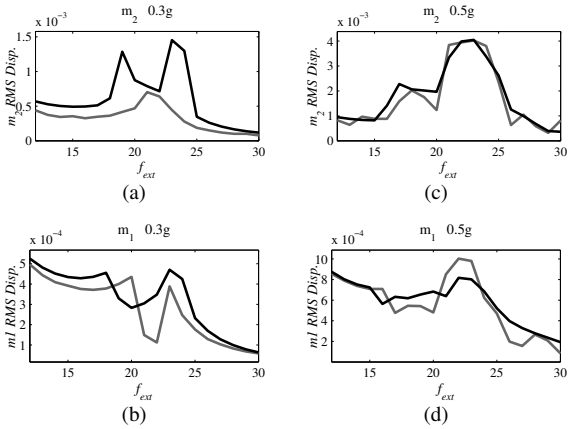

Figure 3: Fitting results of parameters set 2 of conventional model. Grey lines represent experimental data and black lines are simulation results. (a) m_2 under A_{ext} = 0.3 g, (b) m_1 under A_{ext} = 0.3 g, (c) m_2 under A_{ext} = 0.5 g, (d) m_1 under A_{ext} = 0.5 g.

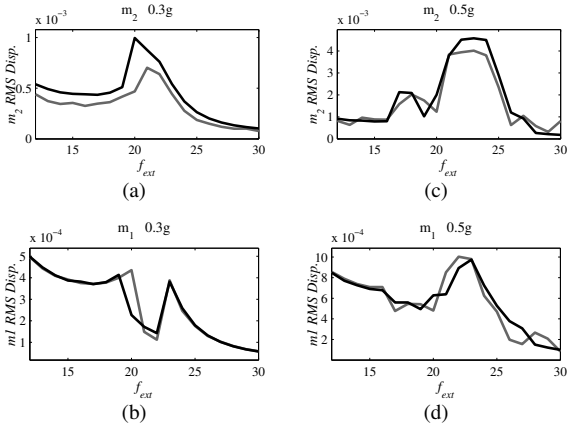

Figure 4: Fitting results of proposed model with Coulomb damping. Grey lines represent experimental data and black lines are simulation results. (a) m_2 under A_{ext} = 0.3 g, (b) m_1 under A_{ext} = 0.3 g, (c) m_2 under A_{ext} = 0.5 g, (d) m_1 under A_{ext} = 0.5 g.

A bifurcation diagram of local maximum value of mass m_2 has been obtained from simulation by keeping A_{ext} = 0.5g while making a frequency sweep from 12Hz to 30Hz as shown in Fig.5a. The sampled local maximum points are derived from 200 external cycles after 500 external cycles of transient time. T-periodic orbit can be observed when the external frequency f_{ext} < 16Hz or f_{ext} > 28Hz which can be expected because the resonator kept working in attached-vibration region so there was no switching occurred within this range.

Correspondingly, nT-periodic orbit can be observed in most situations where the switching between the different configurations occurred. For example, 3T-periodic orbit is shown in Fig.5b and a chaotic orbit is shown in Fig.5c. But there is still some T-periodic orbits existing even when the switching occurred.

Similarly, another bifurcation diagram of mass m_2 was obtained from simulation by keeping f_{ext} = 21Hz while

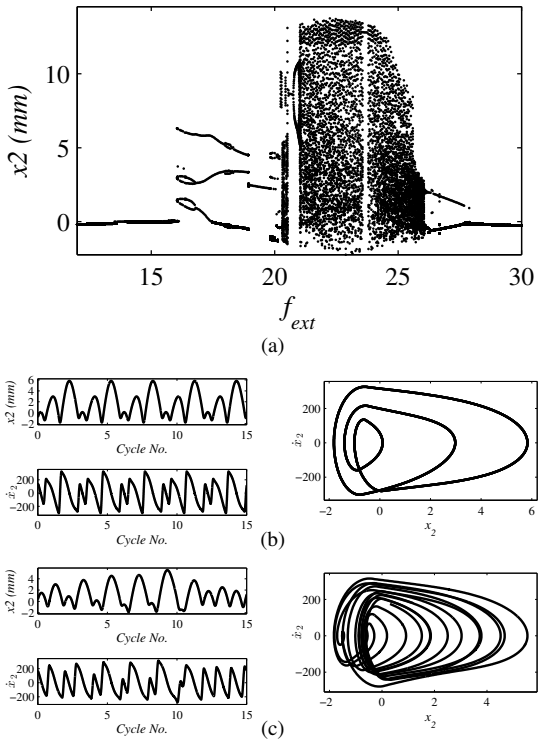

Figure 5: A_{ext} = 0.5 g (a) Bifurcation diagram of local maximum value of mass m_2 over the 12 Hz to 30 Hz external frequency range. (b) Time domain waveform and state space trajectory under f_{ext} = 17.4 Hz. (c) Time domain waveform and state space trajectory under f_{ext} = 20.5 Hz.

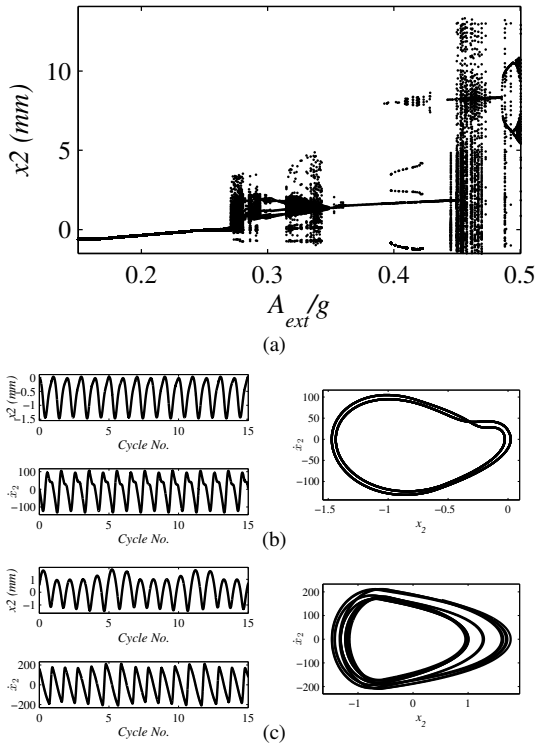

Figure 6: f_{ext} = 21 Hz (a) Bifurcation diagram of local maximum value of mass m_2 over the 0.15 g to 0.5 g external acceleration levels. (b) Time domain waveform and state space trajectory under A_{ext} = 0.27 g. (c) Time domain waveform and state space trajectory under A_{ext} = 0.31 g.

making an external amplitude sweep from 0.15g to 0.5g as shown in Fig.6a. These nonlinear behaviour existing in this 2-DOF resonator means that the prediction of the average displacement could be more useful than the prediction emphasizing the short term trajectory.

4. Conclusion

In this work, three different data fitting results between simulation and experiment has been shown. Two of them are derived from the conventional 2-DOF resonator model and the other one is derived from a proposed 2-DOF resonator model with Coulomb damping. The fitting analysis shows that the proposed model can predict the real systems behaviour much better by using the fixed fitting parameters compared to the conventional model.

In this work, two bifurcation diagrams of the resonator are also presented. One is for swept external frequency with fixed amplitude and another is for swept external amplitude with fixed frequency. Both of them show a rich variety of nonlinear behavior.

References

[1] S. H. Jeon and J. Y. Lee, "Two-mass system with wide bandwidth for siog (silicon on glass) vibratory gyroscopes," in *Solid-State Sensors, Actuators and Microsystems, 2005. Digest of Technical Papers. TRANSDUCERS '05. The 13th International Conference on*, vol. 1, June 2005, pp. 539–542 Vol. 1.

[2] C. Acar and A. Shkel, "Inherently robust micromachined gyroscopes with 2-dof sense-mode oscillator," *Microelectromechanical Systems, Journal of*, vol. 15, no. 2, pp. 380–387, April 2006.

[3] L. Tang and Y. Yang, "A multiple-degree-of-freedom piezoelectric energy harvesting model," *Journal of Intelligent Material Systems and Structures*, vol. 23, no. 14, pp. 1631–1647, 2012.

[4] O. Aldraihem and A. Baz, "Energy harvester with a dynamic magnifier," *Journal of Intelligent Material Systems and Structures*, vol. 22, no. 6, pp. 521–530, 2011.

[5] K. J. Kim and F. Cottone, "Energy scavenging for energy efficiency in networks and applications," *Bell Labs Technical Journal*, vol. 15, no. 2, pp. 7–29, 2010.

[6] X. Li, R. Lin, and K. W. Leow, "Performance-enhanced micro-machined resonant systems with two-degrees-of-freedom resonators," *Journal of Micromechanics and Microengineering*, vol. 10, no. 4, p. 534, 2000.